Electronic Supplementary Material (ESI) for Journal of Materials Chemistry A.

Supporting Information

Ångström-level d-spacing controllable synthetic route for MoS2 towards stable intercalation of sodium ions

Kan Zhang[†a,b*], Ping Li[†b,c], Shiying Guo[a], Jong Yeob Jeong[b], Bingjun Jin[b], Xiaoming Li[a], Shengli Zhang[a], Haibo Zeng[a*] and Jong Hyeok Park[b*]

[a] MIIT Key Laboratory of Advanced Display Materials and Devices, Institute of Optoelectronics and Nanomaterials, School of Materials Science and Engineering, Nanjing University of Science and Technology, Nanjing 210094, People's Republic of China

[b] Department of Chemical and Biomolecular Engineering, Yonsei University, 50 Yonsei-ro, Seodaemun-gu, Seoul 120-749, Republic of Korea

[c] SKKU Advanced Institute of Nano Technology (SAINT), Sungkyunkwan University, Suwon, 440-746, Republic of Korea

† These authors contributed equally to this work

Corresponding Author:

Email: zhangkan@njust.edu.cn;
Email: zeng.haibo@njust.edu.cn
Email: lutts@yonsei.ac.kr

Experimental Section:

Materials

Graphite powder (99.9995% purity) was obtained from Alpha Aesar. All chemical reagents were purchased from Aldrich without further purification.

Synthesis of MoS_2-SA/N-RGO

GO was prepared using Hummer's method and re-dispersed in DMF at a concentration of 3 mg/mL. Then, 0.15 g of $Na_2MoO_4 \cdot 2H_2O$ was dissolved in 4 mL of deionized water, followed by the addition of 2 g of L-cysteine with vigorous stirring. Next, 20 mL of DMF and 10 mL of the GO/DMF solution were mixed. Subsequently, 1 mL of NH_4OH was dropped into the above mixture to form a gel precursor with further stirring for 30 min. The reaction mixture was transferred to a 40 mL Teflon-lined autoclave and maintained at 200 °C for 12 h at a heating rate of 30 °C/min in an electronic oven. Following completion of the reaction, VO-MoS_2/N-RGO was collected via centrifugation and washed several times with water and ethanol. The solid product was heated to 150, 250, 350, 450 or 800 °C with heating rate of 50 °C/min under Ar atmosphere. Once the temperature raised to a setting value, the heating process was immediate-ly modulated to naturally cooling process. Control experiments were carried out by replacing the chemical reagent and keeping the other parameters constant.

Analytical instruments

Scanning electron microscopy (SEM) images of the product were taken on a field emission scanning electron microscope (FE-SEM, JSM-7800F, Japan). XRD patterns were obtained with a diffractometer (D500/5000) in Bragg-Brentano geometry under Cu Kα radiation. HAADF-STEM and the corresponding EELS mapping analyses were performed on a JEOL JEMARM200F TEM/STEM (200 kV) with a spherical aberration corrector. X-ray photoelectron spectroscopy

(XPS) was conducted on an AES-XPS instrument (Escalab 220i-XL) equipped with an aluminum anode (Al Kα = 1486.6 eV). Thermogravimetric analysis (TGA) was conducted using a Seiko Exstar 6000 in an air atmosphere at a heating rate of 1 °C /min. Raman spectra were measured using a LabRam Aramis equipment (Horriba Jovin Yvon Inc., US).

Electrode preparation and electrochemical tests

The composite electrodes were prepared by mixing the powder sample, carbon black (Super P), and carboxymethyl cellulose dissolved in water in a weight ratio of 80:10:10. Carbon black was used as a conductive additive, and carboxymethyl cellulose was added as a binder. The mixed active material was deposited with a thickness of ~35 μm on aluminum foil (~8.6 mg/cm^2), which was used as a current collector, and vacuum dried at 120 ℃ for 12 hours. The electrolyte for the cell was $NaClO_4$ (1 M) with ethylene carbonate (EC)/diethylene carbonate (DEC)/ethyl-methyl carbonate (EMC) (1:1:1 (v/v/v), Techno SEMICHEM Co., Ltd., Korea). All cells were constructed and handled in an Ar-filled glove box. The electrochemical properties were examined in two-electrode cells using an electrochemical analyzer (CHI 608), and Na metal was used as the counter and reference electrodes. The potentiostatic mode was used to measure the electrochemical impedance spectra (EIS) in a frequency range of 0.01-100 kHz.

Theoretical simulations

Theoretical calculations were performed based on density functional theory (DFT) as implemented in the $DMol_3$ code from the Materials Studio package.[1,2] We used the Perdew-Burke-Ernzerhof (PBE) exchange-correlation functional that includes van der Waals corrections. In addition, we chose the double numerical plus polarization (DNP) to expand the electronic wave function. All structures were optimized until the maximum force and energy were lower than 0.002 Ha/Å and 10^{-5} Ha, respectively, to ensure the reliability of the results.

All the systems were modeled using a 4×4×1 supercell. A vacuum space of 18 Å in the direction perpendicular to the plane was applied to avoid the spurious interactions induced by periodic images. The Brillouin zone was sampled using 4×4×1 for the structure relaxation. The Na ion-diffusion barrier was searched and optimized by using the complete LST/QST method. The structures of the initial and final points were fully optimized before the complete LST/QST calculation. The calculation was performed based on the abovementioned details and conditions.

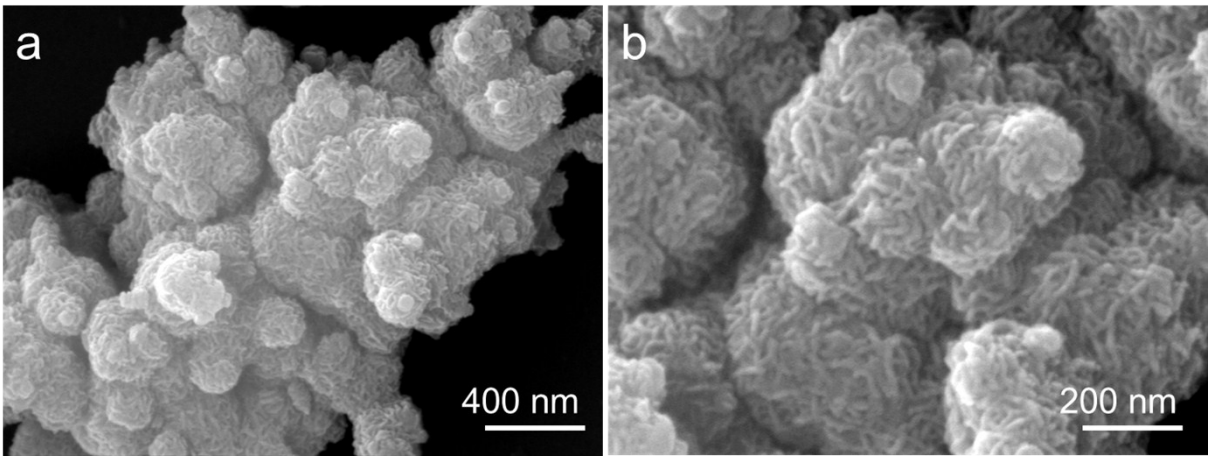

Fig. S1 FE-SEM images of the as-prepared MoS_2 flowers.

The method for synthesis of MoS_2 flowers is similar to that for synthesis of MoS_2-SA/N-RGO except for use of GO.

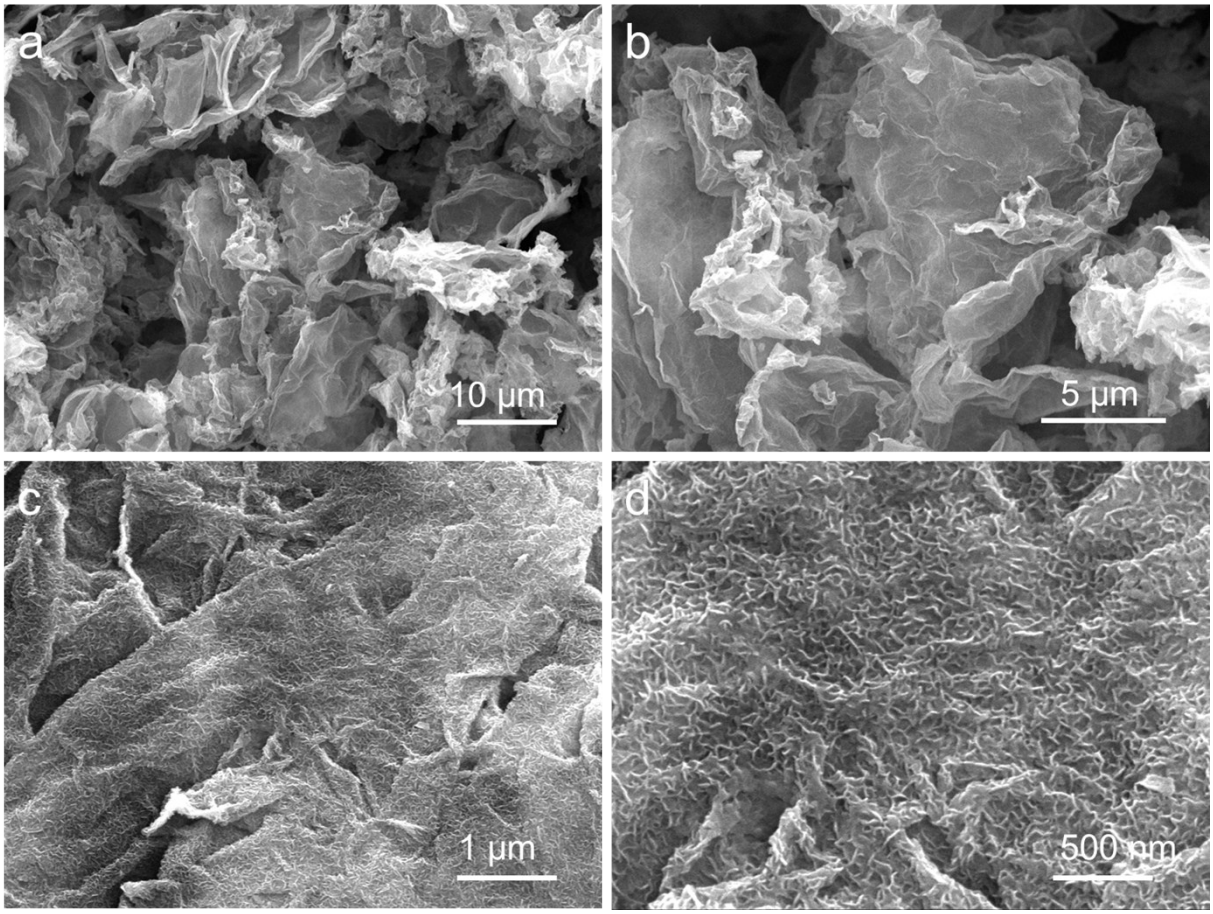

Fig. S2 SEM images of the as-prepared MoS_2-SA/N-RGO without further thermal annealing.

The FE-SEM images with different magnifications confirm a lateral structure, such as an epitaxial or stacked relationship, was not present between the MoS_2 and RGO sheets (Fig. S2). Therefore, the MoS_2 growth on the RGO sheets can be reasonably considered to be isotropic.

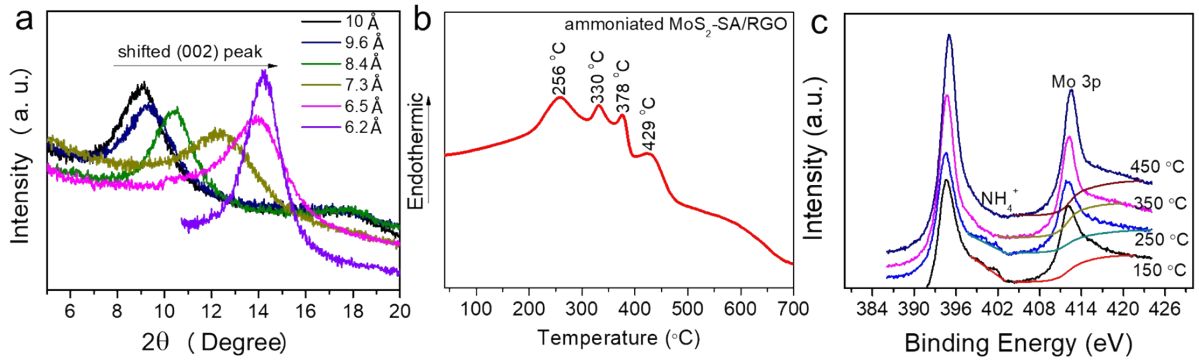

Fig. S3 (a) Enlarged XRD patterns ranging from 5 to 20 degree. (b) Differential thermal analysis of the as-prepared MoS_2-SA/N-RGO without further thermal annealing. (c) N 1s XPS spectra of MoS_2-SA/N-RGO at different heating temperatures.

Ammoniated chalcogenides, such as layered TaS_2 and NbS_2, were studied in the 1970s [3]. The ammoniated MoS_2 obtained in the presence of an RNH_3^+ precursor typically has an interlayer spacing of ~10 Å [4,5]. The ammoniated MoS_2-SA/N-RGO (Fig. S3b) shows four endothermic peaks at 256, 330, 378 and 429 °C, and the N 1s XPS spectra of Mo_{S2}-SA/N-RGO heated at 150, 250, 350 and 450 °C show a gradual disappearance of the N peak (Fig. S3c). According to previous reports on osmotically swollen, ammoniated MoS_2, the first three endothermic peaks below 400 °C can be ascribed to losses of H_2O molecules, NH_3 and NH_4^+ [5-7]. The final endothermic peak at 450 °C is associated with the structure conversion [7].

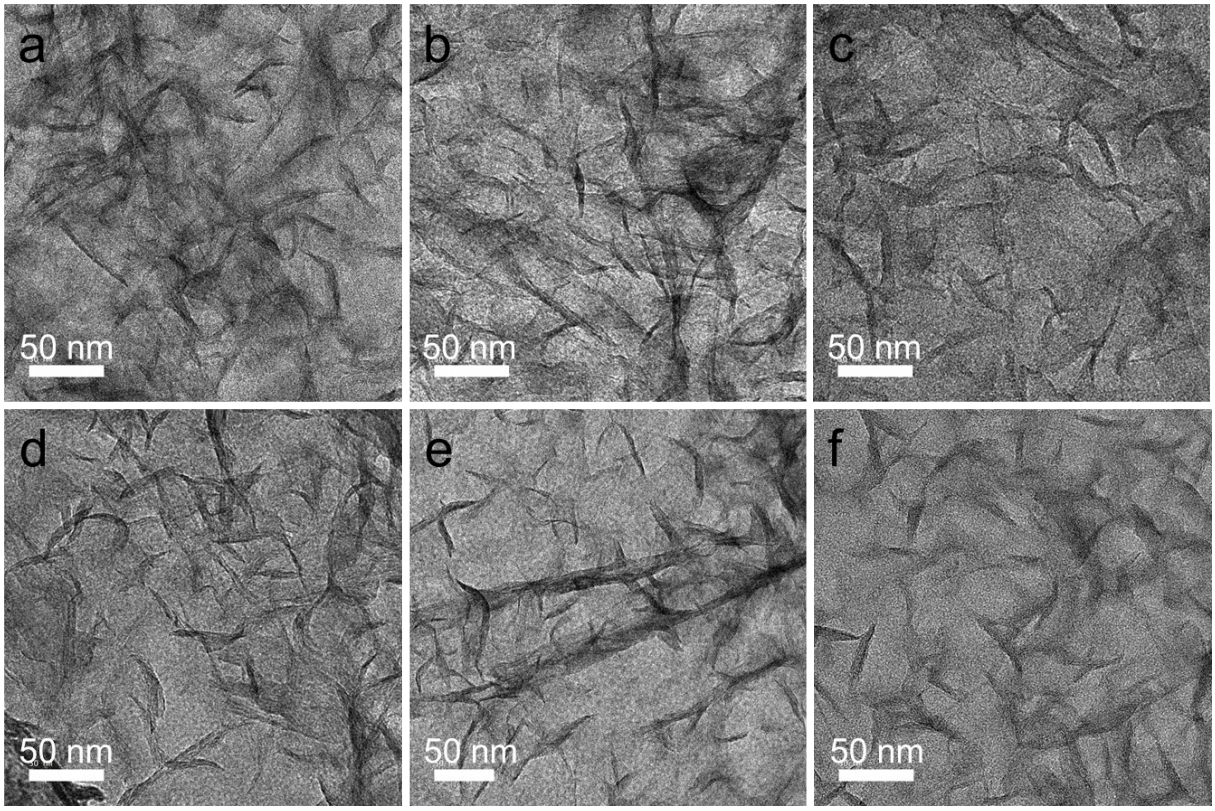

Fig. S4 TEM images of MoS_2-SA/N-RGO samples heated at different temperatures. a: pristine sample with a d-spacing of 10 Å, b: annealed at 150 °C with a d-spacing of 9.6 Å, c: annealed at 250 °C with a d-spacing of 8.4 Å, d: annealed at 350 °C with a d-spacing of 7.3 Å, e: annealed at 450 °C with a d-spacing of 6.5 Å, f: annealed at 800 °C with a d-spacing of 6.2 Å.

Element	Wt%	Wt% Sigma	Atomic %
C	10.16	0.53	33.12
N	0.41	0.00	1.16
S	36.04	0.69	43.59
Mo	53.39	0.74	21.77
Total:	100.00		100.00

Fig. S5 STEM-EDX pattern of major element MoS_2-SA/N-RGO sample after being annealed at 800 °C. We assumed that the residual N as dopant is originating from RGO sheet, therefore, the N weight percent is roughly calculated based on $N\ wt.\% = \frac{N\ content}{C\ content + N\ content}$.

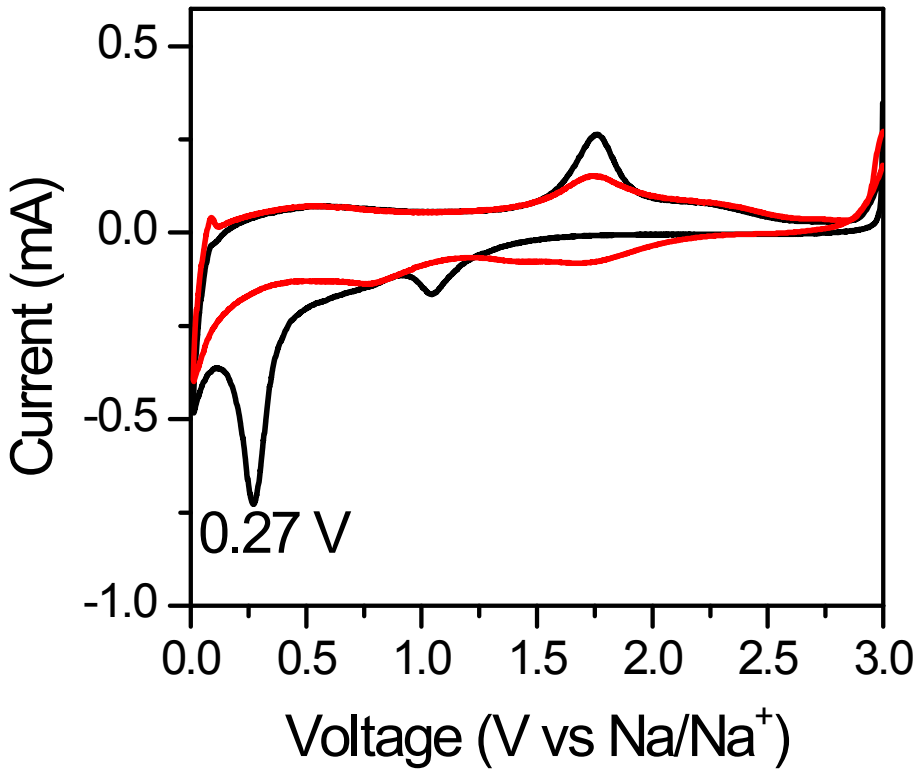

Fig. S6 CV curves of MoS_2-SA/N-RGO in a voltage region between 0.01 and 3 V vs. Na/Na^+; a reduction peak is seen at 0.27 V in the first cycle (black line), which disappears in the second cycle (red line), can correspond to an irreversible reaction for formation of SEI layer.

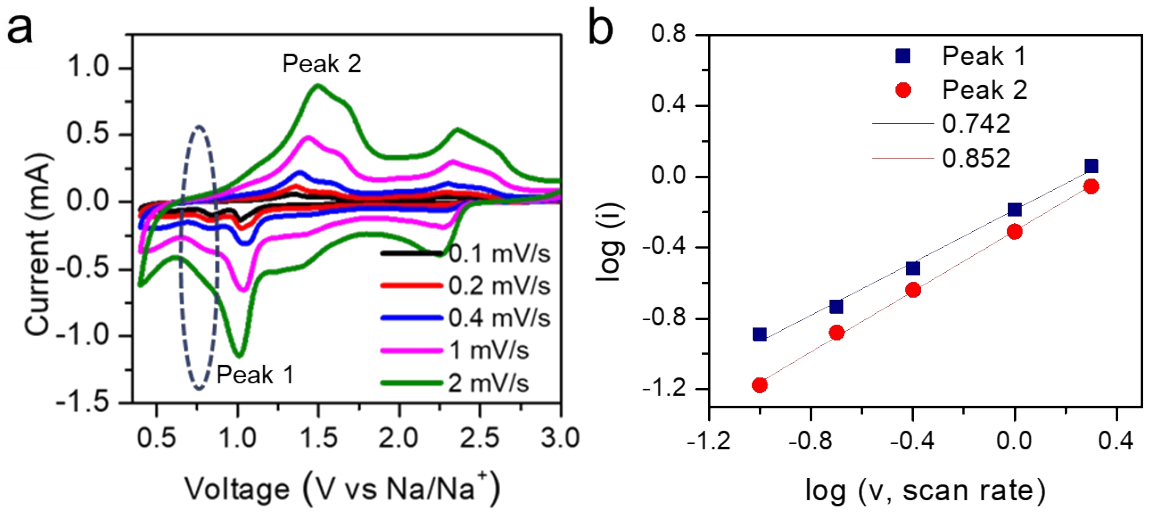

Fig. S7 (a) CV curves of bulk MoS_2 in the voltage region between 0.4 and 3 V vs. Na/Na^+ at different scanning rates. (b) log *i* vs log *v* plotted by redox peaks of their CV curves.

The charge storage mechanism of intercalation includes non-faradaic and faradaic processes, which can be calculated according to the following equations:

$i = a v^b$ (1)

$\log i = b \times \log v + \log a$ (2)

where *i* is the current density of redox peak, *v* is the scan rate, and a and b are adjustable parameter. The non-faradaic process can be determined when value of b is close to 0.5, whereas the value of b approaching 1 means faradaic process. The values of b can be calculated to 0.742 for main reduction peak and 0.852 for main oxidation peak. As the values of b is between 0.5 and 1, the capacity of bulk MoS_2 might be controlled by both non-faradaic and faradaic processes. The results also indicate a slow Na^+ insertion/extraction.

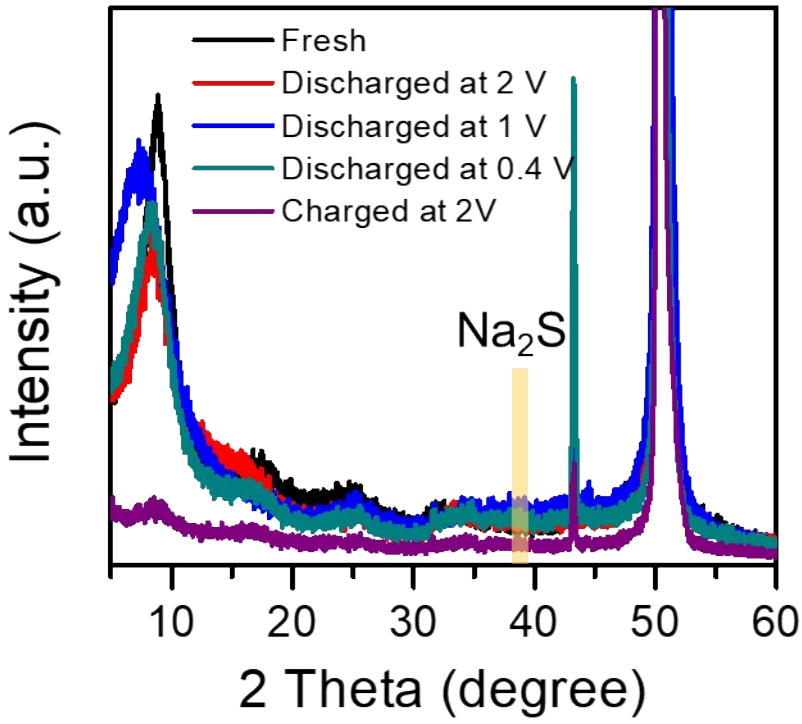

Fig. S8 Ex-situ XRD patterns of MoS_2-SA/N-RGO with d-spacing of 10 Å at different cut off voltages.

When discharged to 2 V, the initial (002) reflection peak at 8.8 ° was decreased in intensity with a little shift toward lower angle. After continuous discharged to 1 V, the (002) reflection peak was shifted to 7.9 °, which was then shifted back to 8.8 ° at discharge voltage of 0.4 V. The blue-shifted peak can be ascribed to Na^+ intercalation at the discharge voltage of 1 V, and the shift back as decreasing discharge voltage to 0.4 V was due to the phase transformation from 2H to 1T. [8] The diffraction peak at $2\theta \approx 38.9$ corresponding to the (220) plane of Na_2S was undetectable. [9] On the basis of above results, the structure and phase of MoS_2-SA/N-RGO electrode can be partially recovered upon Na^+ intercalation.

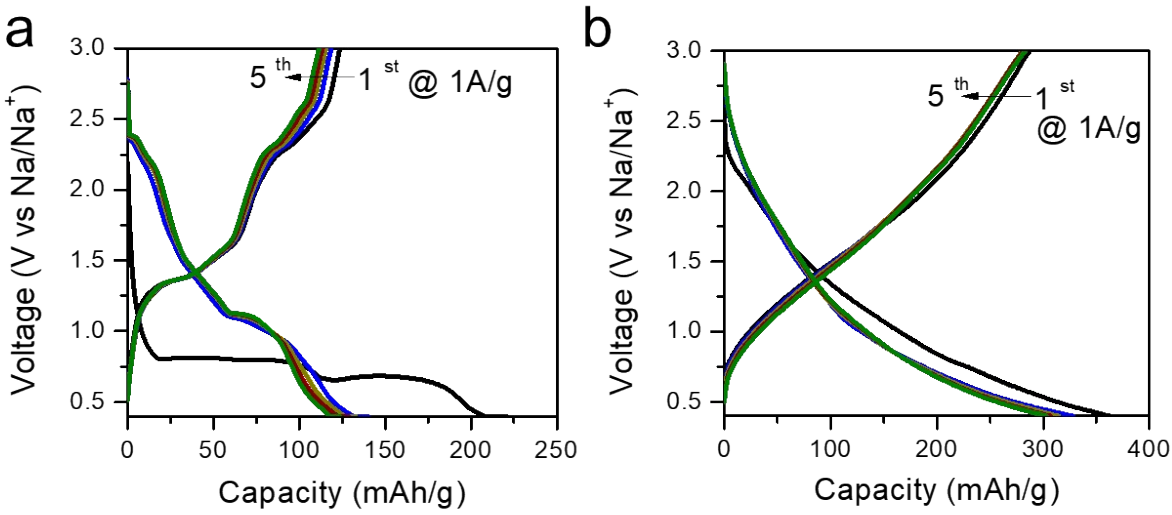

Fig. S9 Charge/discharge profile of Na^+ intercalation in bulk MoS_2 (a) and MoS_2-SA/N-RGO with a d-spacing of 7.3 Å (b).

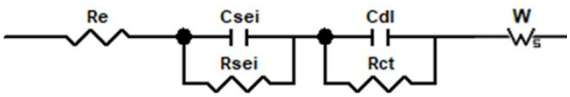

Samples	Re (Ω)	R_{SEI} (Ω)	R_{ct} (Ω)
6.2 Å	9.19	52.06	21.56
6.5 Å	9.38	52.64	12.12
7.3 Å	9.91	51.17	12.1
8.4 Å	10.76	76.87	92.96
9.6 Å	11.33	115.59	813
10 Å	10.77	119.73	1875

Fig. S10 Equivalent circuit and the resistance of MoS_2-SA/N-RGO electrodes calculated by Fig. 4c.

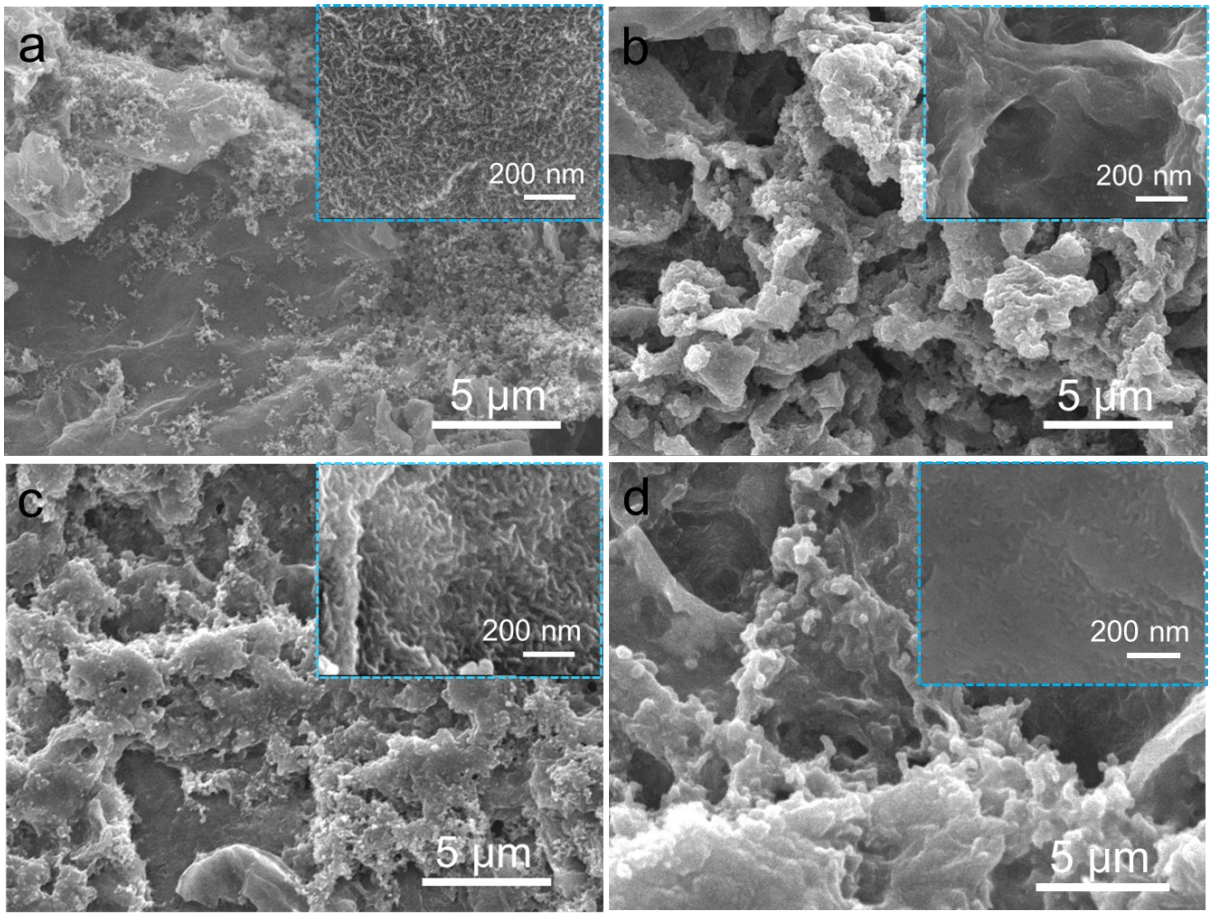

Fig. S11 (a-d) FE-SEM images of the fresh and cycled MoS_2-SA/N-RGO electrodes, (a) fresh electrode with a d-spacing of 7.3 Å, and cycled electrode with d-spacings of 10 Å (b), 7.3 Å (c), 6.2 Å (d). Insets are enlarged FE-SEM images taken from each image surface.

Fig. S11 displays the microstructure of MoS_2-SA/N-RGO, and the inset in Fig. S10a is an FE-SEM image taken of the MoS_2-SA/N-RGO sheet surface. Vertical MoS_2 sheets are obviously present before cycling. For the sample with a d-spacing of 10 Å, the MoS_2 sheets are deeply buried under an SEI layer after 100 cycles (Fig. S11b), whereas for the samples with a d-spacing of 7.3 or 6.2 Å, the vertical feature is detectable (Fig. S11c and S11d). The electrolyte contains strongly solvating groups (carbonyl groups) that arrange as a solvation shell around Na^+ ions, and the diameter of solvated Na^+ should be larger than that of ionic Na^+.[7, 10] Thus, large d-spacing will favor ionic Na^+ diffusion and allow diffusion of solvated Na^+, leading to an extrinsic charge capacity with a lower initial CE in the first cycle.[11] Conversely, a suitable d-spacing can selectively reject solvated Na^+, which will suppress SEI layer formation in the interlayer of MoS_2.

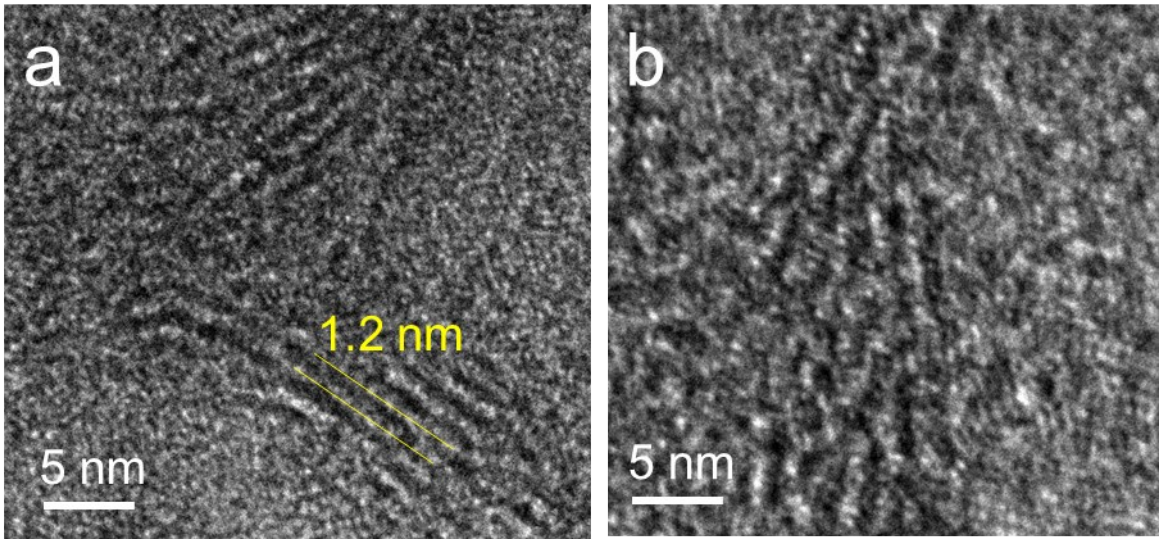

Fig. S12 HR-TEM images of MoS_2-SA/N-RGO with d-spacings of 7.3 and 10 Å after 100 cycles. HR-TEM images show the edge feature of 7.3 Å case still is detectable although the d-spacing increases to 12 Å, whereas the 10 Å case shows disorder feature.

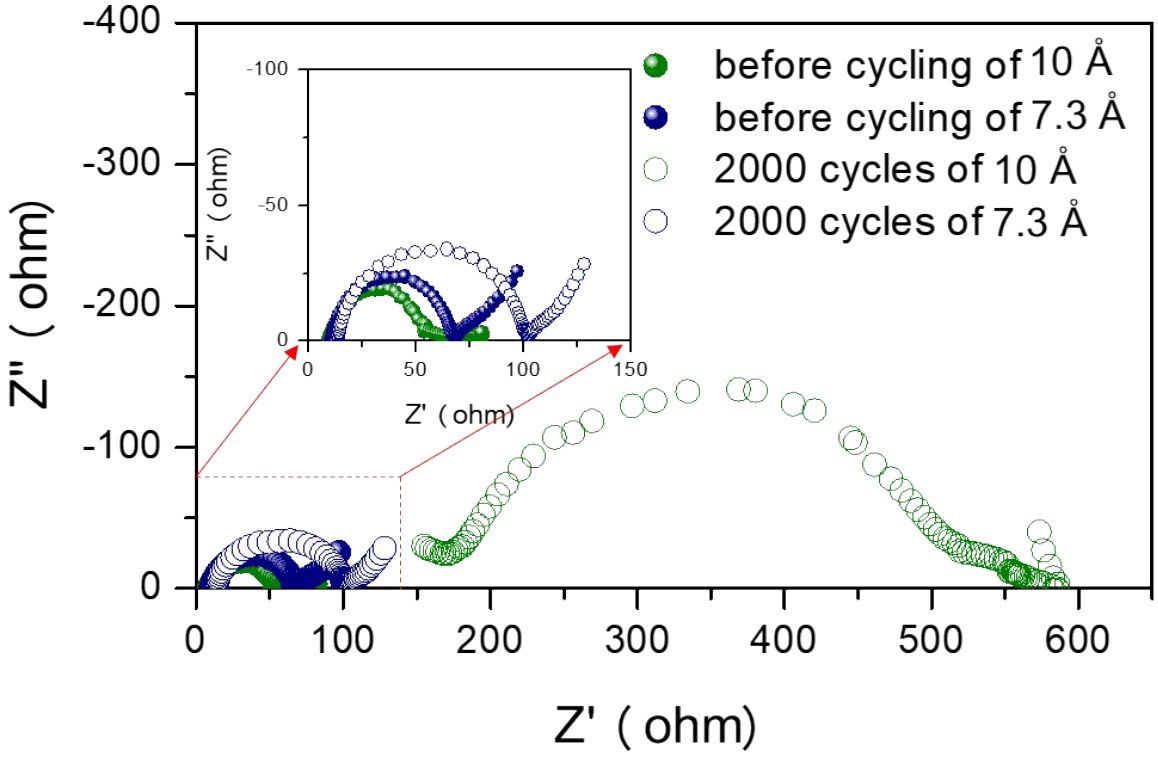

Fig. S13 Electrochemical impedances of MoS_2-SA/N-RGO electrodes with d-spacings of 10 and 7.3 Å before and after cycles.

Equivalent circuit for EIS analysis is similar to Fig. S10. The R_{ct} of 7.3 Å d-spacing increases from 55.2 Ω before cycling to 99 Ω after 2000 cycles. For 10 Å d-spacing, the R_{ct} increases from 40.5 Ω before cycling to 567.1 Ω after 2000 cycles. The remarkably increased R_{ct} for 10 Å case can be ascribed to that irreversible SEI formed inside overly large d-spacing

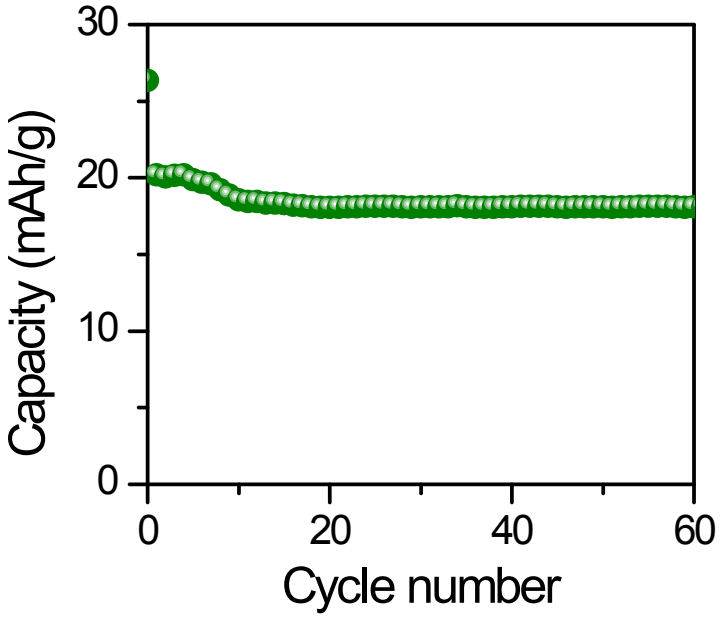

Fig. S14 Cycling performance of N-RGO at current density of 1A/g in the voltage region between 0.4 and 3 V vs. Na/Na^+.

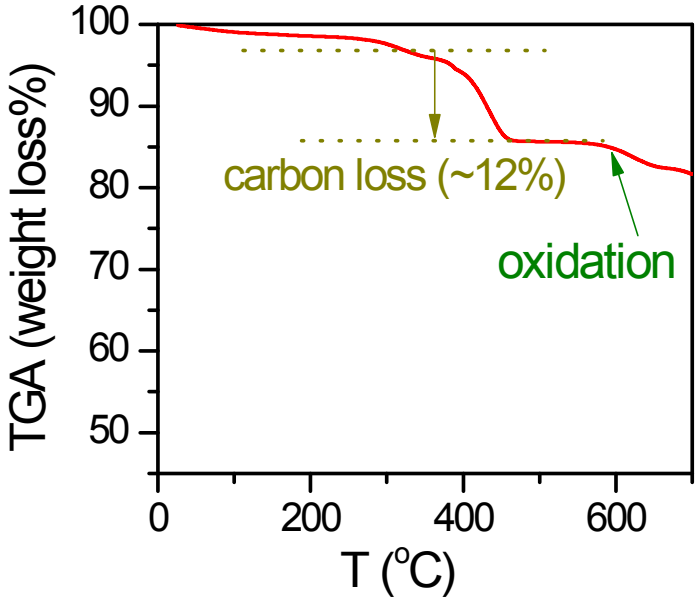

Fig. S15 TGA analysis of MoS_2-SA/N-RGO after being annealed at 800 °C.

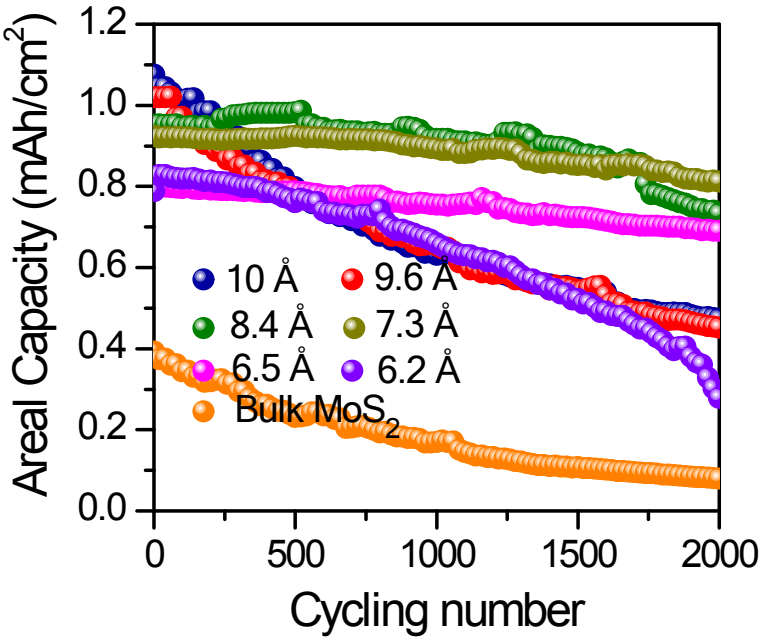

Fig. S16 Area capacities of the MoS_2-SA/N-RGO and bulk MoS_2 electrodes.

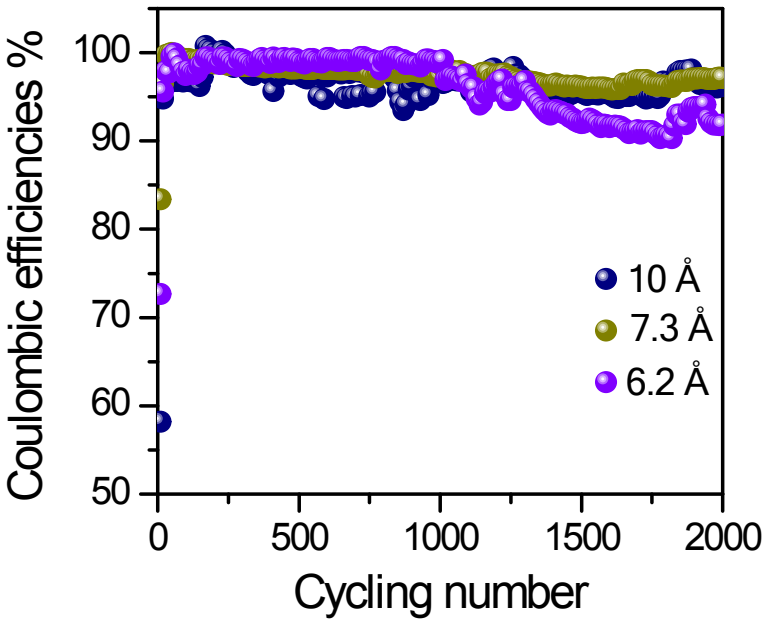

Fig. S17 CEs of the MoS_2-SA/N-RGO electrodes with d-spacing of 10, 7.3 and 6.2 Å.

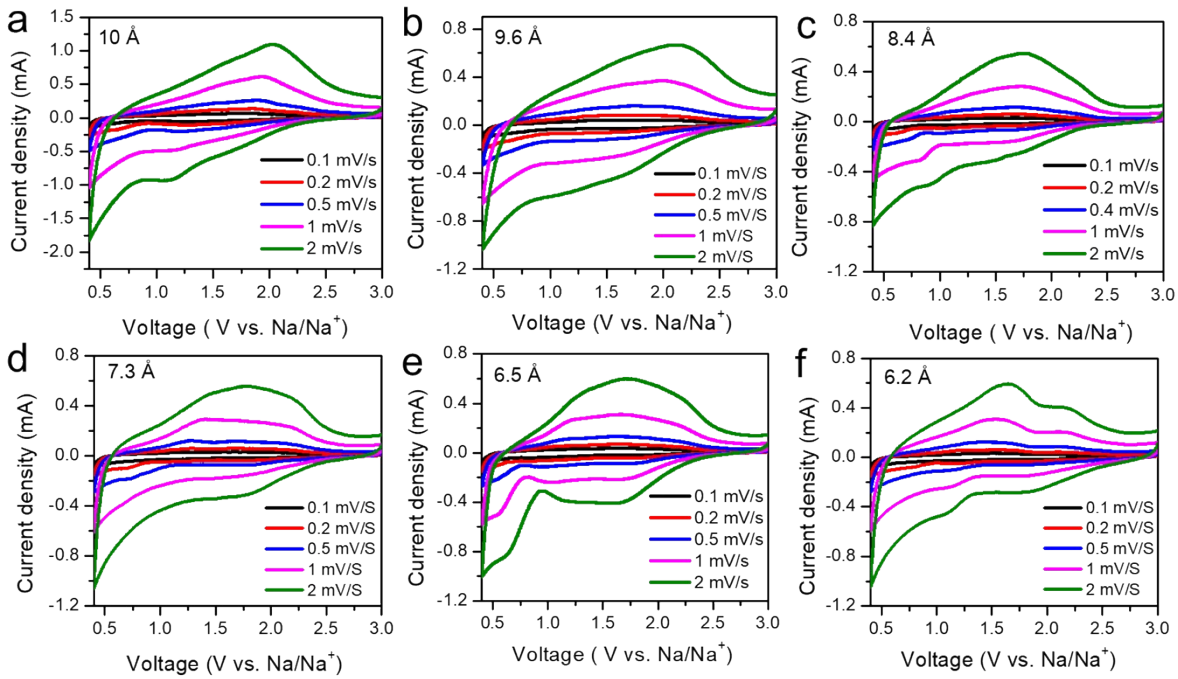

Fig. S18 CV curves of the MoS_2-SA/N-RGO samples in a voltage region between 0.4 and 3 V vs. Na/Na^+.

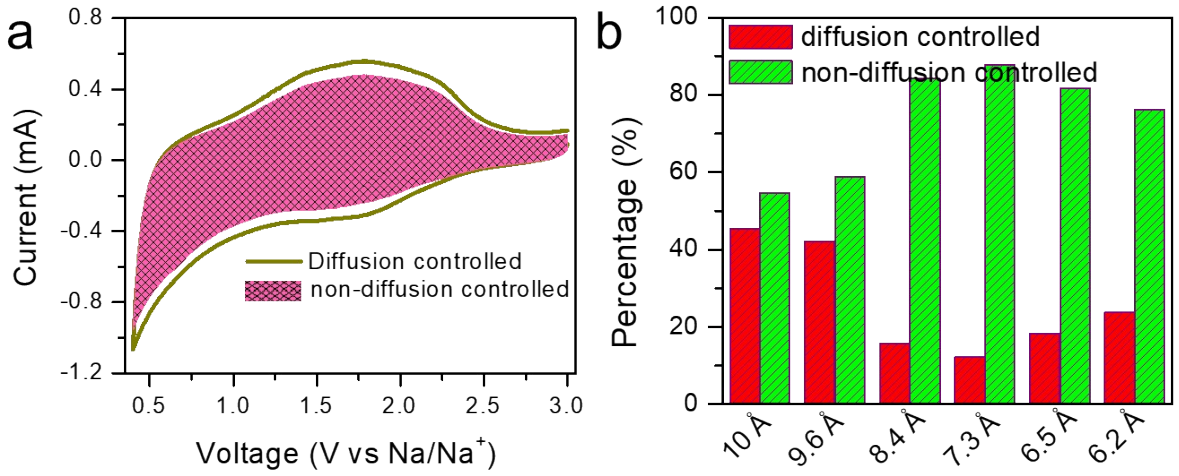

Fig. S19 (a) Non-diffusion-controlled capacity (pink area) contribution to charge storage in MoS_2-SA/RGO with a d-spacing of 7.3 Å at 5 mV/s. (b) Normalized contribution ratio of the diffusion-controlled capacity and non-diffusion-controlled capacity for the MoS_2-SA/RGO electrodes at 5 mV/s.

According to Dunn's reports,[12,13] the capacitive contribution ratio of the pseudocapacitance effect and the electrical double-layer effect can be quantified by separating the current response, *i*, at a fixed potential, *V*,

$$i = k_1 v + k_2 v^{1/2}$$

where the current at a fixed potential is divided into the pseudocapacitance effect ($k_1 v$) and the electrical double-layer effect ($k_2 v^{1/2}$). The CV curves recorded at different scanning rates are shown in Fig. S18. By determining the slope, k_1, and intercept, k_2, at a fixed potential, the current fractions from pseudocapacitance and electrical double-layer capacitance can be obtained. Figure 19a shows a typical CV curve of MoS_2-SA/N-RGO with a d-spacing of 7.3 Å, and the capacitive current (red region) at a scan rate of 5 mV/s indicates 87.8% of the current is contributed by the pseudocapacitance effect. Using a similar calculation, the pseudocapacitance and electrical double-layer effects for MoS_2-SA/N-RGO samples with different d-spacings are summarized in Fig. S19b. The contribution of the non-diffusion-controlled pseudocapacitance effect gradually increases as the d-spacing decreases to 7.3 Å, and then, the contribution decreases as the d-spacing further decreases to 6.2 Å. In general, non-diffusion-controlled processes favor fast and reversible electrochemical reactions that can enable high Na^+ storage performances.

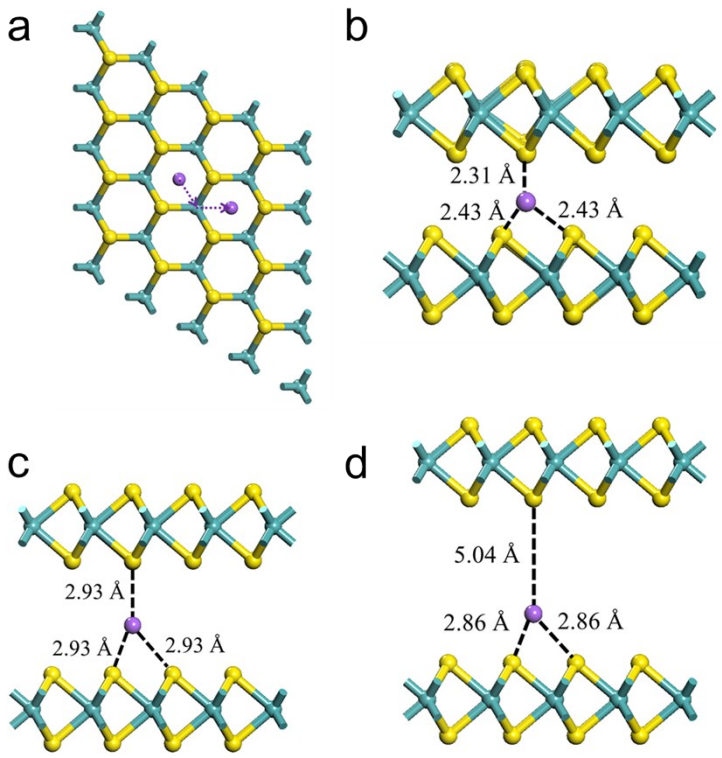

Fig. S20 Theoretical simulation of Na diffusion in MoS_2 with different d-spacings. (a) In-plane diffusion in a monolayer structure; (b) Interlayer diffusion in a bilayer structure with an established d-spacing of 6.15 Å; (c) Interlayer diffusion in a bilayer structure with an established d-spacing of 7.3 Å; (d) Interlayer diffusion in a bilayer structure with an established d-spacing of 10 Å.

Table S1. Recent progress on nanostructured MoS_2 for electrochemical intercalation of Na^+.

Materials	Voltage range (V vs. Na^+/Na)	Cycling data	Rate capability	reference
MoS_2 nanoflowers	0.4–3.0	300/1500th @ 1 A/g	195/10 A/g	s14
MoS_2 nanosheets	0.4–2.6	161/50th @ 0.02 A/g	≈120/0.8 A/g	s15
MoS_2/rGO	0.4–2.6	131/1000th @ 1 A/g	150 @ 1 A/g	s16
MoS_2/C	0.4–3.0	184/1200th @ 1 A/g	148 @ 5 A/g	s17
PEO–MoS_2	0.4–3.0	150/70th @ 0.05A/g	112 @ 1 A/g	s18
MoS2-SA/N-RGO (7.3 Å)	0.4–3.0	295/2000th @ 1 A/g	179 @ 10 A/g	Our work

Reference

s1 J. P. Perdew, K. Burke and M. Ernzerhof, *Physical review letters*, 1996, **77**, 3865.

s2 N. Govind, M. Petersen, G. Fitzgerald, D. King-Smith and J. Andzelm, *Computational materials science*, 2003, **28**, 250-258.

s3 X. Wang, X. Shen, Z. Wang, R. Yu and L. Chen, *ACS nano*, 2014, **8**, 11394-11400.

s4 P. Li, J. Y. Jeong, B. Jin, K. Zhang and J. H. Park, *Advanced Energy Materials*, 2018, 1703300.

s5 F. Gamble, J. Osiecki, M. Cais, R. Pisharody, F. DiSalvo and T. Geballe, *Science*, 1971, **174**, 493-497.

s6 Q. Liu, X. Li, Q. He, A. Khalil, D. Liu, T. Xiang, X. Wu and L. Song, *Small*, 2015, **11**, 5556-5564.

s7 A. Anto Jeffery, C. Nethravathi and M. Rajamathi, *The Journal of Physical Chemistry C*, 2014, **118**, 1386-1396.

s8 Z. Wu, C. Tang, P. Zhou, Z. Liu, Y. Xu, D. Wang and B. Fang, *Journal of Materials Chemistry A*, 2015, **3**, 13050-13056.

s9 D. Wang, Y. Xiao, X. Luo, Z. Wu, Y.-J. Wang and B. Fang, *ACS Sustainable Chemistry & Engineering*, 2017, **5**, 2509-2515.

s10 A. Ponrouch, D. Monti, A. Boschin, B. Steen, P. Johansson and M. Palacin, *Journal of Materials Chemistry A*, 2015, **3**, 22-42.

s11 A. Ponrouch, E. Marchante, M. Courty, J.-M. Tarascon and M. R. Palacin, *Energy & Environmental Science*, 2012, **5**, 8572-8583.

s12 T. Brezesinski, J. Wang, S. H. Tolbert and B. Dunn, *Nature materials*, 2010, **9**, 146.

s13 A. Bard, L. Faulkner, J. Leddy and C. Zoski, 1980.

s14 Z. Hu, L. Wang, K. Zhang, J. Wang, F. Cheng, Z. Tao and J. Chen, *Angewandte Chemie International Edition*, 2014, **53**, 12794-12798.

s15 G. S. Bang, K. W. Nam, J. Y. Kim, J. Shin, J. W. Choi and S.-Y. Choi, *ACS applied materials & interfaces*, 2014, **6**, 7084-7089.

s16. T. S. Sahu and S. Mitra, *Scientific reports*, 2015, **5**, 12571.

s17 J. B. Cook, H. S. Kim, Y. Yan, J. S. Ko, S. Robbennolt, B. Dunn and S. H. Tolbert, *Advanced Energy Materials*, 2016, **6**, 1501937.

s18 Y. Li, Y. Liang, F. C. R. Hernandez, H. D. Yoo, Q. An and Y. Yao, *Nano Energy*, 2015, **15**, 453-461.